Revision 1

A new $(Mg_{0.5}Fe^{3+}_{0.5})(Si_{0.5}Al^{3+}_{0.5})O_3$ $LiNbO_3$-type phase synthesized at lower mantle conditions

Zhaodong Liu [1, 2 *], Leonid Dubrovinsky[1], Catherine McCammon[1], Sergey V. Ovsyannikov[1], Iuliia Koemets[1], Luyao Chen[2], Qi Cui[3], Na Su[3], Jinguang Cheng[3, 4], Tian Cui [2], Bingbing Liu [2], Tomoo Katsura[1,5]

[1]Bayerisches Geoinstitut, University of Bayreuth, Bayreuth 95440, Germany.

[2] State Key Laboratory of Superhard Materials, Jilin University, Changchun 130012, China

[3]Beijing National Laboratory for Condensed Matter Physics and Institute of Physics, Chinese Academy of Sciences, Beijing 100190, China.

[4]Songshan Lake Materials Laboratory, Dongguan, Guangdong 523808, China.

[5]Center for High Pressure Science and Technology Advanced Research, Beijing, 100094, P.R. China

* Corresponding author: Zhaodong Liu (liu_zhaodong@jlu.edu.cn)

Abstract

A new $(Mg_{0.5}Fe^{3+}_{0.5})(Si_{0.5}Al^{3+}_{0.5})O_3$ $LiNbO_3$-type phase was synthesized at 27 GPa and 2000 K under highly oxidized conditions using an advanced multi-anvil apparatus. Single crystals for this phase are 0.2-0.3 mm in dimension and maroon in color. They crystallize in a noncentrosymmetric structure with space group *R*3*c* and lattice parameters of a = b = 4.8720 (6) Å, c = 12.898 (2) Å, and V =265.14 (8) Å^3. Fe^{3+} and Al^{3+} cations substitute into *A* (Mg^{2+}) and *B* (Si^{4+}) sites through charge-coupled substitution mechanism, respectively. The distortion of BO_6 (B = $Si_{0.5}Al^{3+}_{0.5}$) octahedra is 1.6 times higher than that of AO_6 (A = $Mg_{0.5}Fe^{3+}_{0.5}$) octahedra. This phase is probably recovered from bridgmanite at lower-mantle conditions by a diffusionless transition because of the displacement of A cations and distortion of BO_6 octahedra on releasing pressure. Bridgmanite can thus contain the $FeAlO_3$ component (50 mol%) beyond previously reported solubility limit (37 mol%). The present study shows that the Earth's most abundant elements form a new Fe^{3+}- and Al^{3+}-rich $LiNbO_3$-type compound from bridgmanite at lower mantle conditions. This new compound provides a new insight into the complicated crystal chemistry of $LiNbO_3$-type phase/bridgmanite and constrains the pressure and temperature conditions for shocked meteorites.

Keywords: $LiNbO_3$-type, single crystals, bridgmanite, crystal chemistry, lower mantle

INTRODUCTION

Phase compositions of ABO_3 compounds are of great significance in physics, chemistry, and geoscience. Among ABO_3 compounds, $LiNbO_3$ (*LN*)-type compounds exhibit remarkable physical properties because of their noncentrosymmetric structure (space group: $R3c$) and capacity to adopt a multitude of distortions between BO_6 and AO_6 octahedra (Navrotsky et al., 1998). Some *LN*-type oxides such as $LiNbO_3$ and $LiTaO_3$ can be prepared at ambient conditions (Megaw, 1968; Abrahams and Bernstein, 1967), whereas the majority of *LN*-type oxides have been regarded as a metastable quench phase formed from high-pressure stable orthorhombic perovskite by a diffusionless transformation upon decompression (e.g., Ross et al., 1989; Leinenweber, 1991; Navrotsky et al., 1998; Ishii et al. 2017). Natural *LN*-type $FeTiO_3$ was also discovered in shocked gneiss from the Ries impact crater, southern Germany (Dubrovinsky et al., 2009), and can be used an indicator for shock conditions (Akaogi et al., 2016). Consequently, synthesis of new *LN*-type compounds and exploration of the novel functionalities related to their structures are important in Earth and planetary science as well as and physics and material science.

$MgSiO_3$ perovskite (bridgmanite) is one of the most common ABO_3 phases in the Earth's mantle, and can contain a large amount of Fe^{3+} in the presence of Al^{3+} (McCammon, 1997; Frost and Langenhorst, 2002). The incorporation of Fe^{3+} and Al^{3+} would great change the physical and chemical properties of bridgmanite such as elasticity (*e.g.*, Boffa Ballaran et al., 2012), electrical conductivity (*e.g.*, Yoshino et al., 2016), and Mg-Fe partitioning in the lower-mantle phases (Frost and Langenhorst, 2002). Several studies have found that $MgSiO_3$ bridgmanite with the Al_2O_3 contents above 25 mol% would transform to the *LN*-type phase upon releasing pressure (Funamori et al., 1997; Miyajima et al., 1999; Liu et al., 2016, 2017a; Ishii et al., 2017). The

presence of Al^{3+} can also enhance the incorporation of Fe^{3+} to form the charge-coupled $FeAlO_3$ component in bridgmanite through the following reaction: $Al_2O_3 + 3Fe^{2+}O = 2Fe^{3+}AlO_3 + Fe^0$ (Frost and Langenhorst, 2002). The effective ionic radius of Fe^{3+} (0.645 Å) in six-fold coordination is significantly larger than that of Al^{3+} (0.535 Å) and Si^{4+} (0.40 Å) but close to that of Mg^{2+} (0.72 Å) (Shannon, 1976). In principle, Fe^{3+} preferentially substitutes on the *A* (Mg^{2+}) site rather than the *B* (Si^{4+}) site due to comparable cation sizes. It is thus expected that $FeAlO_3$-bearing *LN*-type phases can be synthesized at lower mantle conditions and exhibit similar or distinct physical and chemical properties with only Al-bearing *LN*-type phases. However, such issues remain poorly understood.

Here, we report a new *LN*-type compound $(Mg_{0.5}Fe^{3+}_{0.5})(Si_{0.5}Al^{3+}_{0.5})O_3$ with *R*3*c* symmetry synthesized at 27 GPa and 2000 K in a multi-anvil press. We investigate the crystal structure of the *LN*-type phase by means of single crystal X-ray diffraction, electron probe microanalyzer, and Mössbauer spectroscopy. Finally, we discuss the crystal chemistry of the *LN*-type phase and its implications for the mineralogy of the lower mantle and the pressure and temperature conditions of shocked meteorites.

EXPERIMENTAL METHODS

A fine-grained oxide mixture with a bulk composition 50 mol% $MgSiO_3$ plus 50 mol% $FeAlO_3$ was used as the starting material, which was prepared from reagent-grade oxide powders of MgO, SiO_2, Al_2O_3, and Fe_2O_3 with a grain size smaller than 1 μm. The starting material was loaded into a platinum capsule, heated at 800 K for one hour, and then welded. This procedure is expected to maintain $Fe^{3+}/\sum Fe = 100\%$ and minimize absorbed water. Quench experiments were

performed at 27 GPa and 2000 K for 20 hours using a Cr_2O_3-doped MgO octahedron with a 7-mm edge length and $LaCrO_3$ sleeve for heating in combination with tungsten carbide cubes with 3-mm truncated edge lengths in a Kawai-type multi-anvil apparatus (IRIS-15) with a press load of 15 MN at the Bayerisches Geoinstitut, University of Bayreuth (Ishii et al., 2016; Liu et al. 2017b).

Phases in recovered samples were initially identified using a micro-focused X-ray diffraction (MXRD) with a Co anode operated at 40 kV and 500 mA. Back-scattered electron (BSE) images were obtained using a LEO1530 scanning electron microscope (SEM). Phase compositions were analyzed using a JEOL JXA-8200 electron probe microanalyzer (EPMA) operating at an acceleration voltage of 15 kV and a beam current of 5 nA with standards of enstatite for Mg and Si and corundum for Al. A high-quality single crystal of ~0.04 mm in diameter was selected for single crystal X-ray diffraction (SXRD) and the data were collected at ambient conditions using a three-circle diffractometer equipped with a SMART APEX CCD detector and a high-brilliance Iμs 3.0 microfocus anode (Ag radiation). The exposure time was 10 s per frame. Lorentz and polarization corrections as well as an analytical absorption correction based on the crystal shape were taken into account for the correction of the reflection intensities using the CrysAlis package (Oxford Diffraction 2017). All crystallographic data refinements were performed based on F^2 using the SHELX97 program package (Sheldrick, 2008) in the WinGX System (Farrugia, 1999). The $Fe^{3+}/\Sigma Fe$ ratio was measured using Mössbauer spectroscopy on one the same single crystal, which was conducted in transmission mode on a constant acceleration Mössbauer spectrometer with a nominal 370 MBq ^{57}Co point source in a 12 mm Rh matrix. The velocity scale was calibrated relative to α-Fe. Detailed information can be found in McCammon (1994) .

RESULTS AND DISCUSSIONS

The MXRD pattern of the recovered sample indicates that all diffraction peaks can be matched to those of an *LN*-type phase (Fig. 1a). A BSE image further confirms that the run product consists of only a single phase with grain sizes on the order of 0.2-0.3 mm (Fig. 1b). Optical microscope observations show that the crystals are translucent, maroon in color, and free of visible imperfections (Fig. 1c). The room temperature Mössbauer spectrum of the sample (Fig. 1d) can be fit to one doublet. The hyperfine parameters, center shift (CS) and quadruple splitting (QS), are 0.34 ± 0.01 and 0.91 ± 0.01 mm/s, respectively. These values are in good agreement with Fe^{3+} in silicate perovskite with CS of ~0.3 mm/s and QS of 0.73–0.94 mm/s (McCammon, 1997; Lauterbach et al. 2000). However, a doublet with high CS and QS characteristic of Fe^{2+} in silicate perovskite is not observed. The $Fe^{3+}/\Sigma Fe$ value is thus 100% within analytical uncertainty, suggesting a pure Fe^{3+}-bearing *LN* phase. EPMA shows that the *LN*-type phase has a composition of $(Mg_{0.49 \pm 0.01}Fe^{3+}_{0.49 \pm 0.01}Al^{3+}_{0.02 \pm 0.01})(Si_{0.50 \pm 0.01}Al^{3+}_{0.50 \pm 0.01})O_{3.01 \pm 0.01}$. Because the effective ionic radius of Fe^{3+} (0.645 Å) in six-fold coordination is closer to that of Mg^{2+} (0.72 Å) rather than to that of Si^{4+} (0. 40 Å), and the radius of Al^{3+} (0.535 Å) is closer to that of Si^{4+}, Fe^{3+}, and Al^{3+} are expected to substitute for Mg^{2+} (*A* site) and Si^{4+} (*B* site), respectively, through a charge-coupled substitution (Fe^{3+} (*A*) + Al^{3+} (*B*) = Mg^{2+} (*A*)+ Si^{4+} (*B*)). But we note that a small fraction of Al^{3+} may be present on the *A* site (within the uncertainty of the measurements) due to an excess of Al. These results will be discussed below based on the results of SXRD refinement.

Crystallographic data for the *LN*–type $(Mg_{0.5}Fe^{3+}_{0.5})(Si_{0.5}Al^{3+}_{0.5})O_3$ phase from the SXRD refinement can be found in the deposited CIF. The lattice parameters and volume are a = b = 4.8720 (6) Å, c = 12.898 (2) Å, and V =265.14 (8) $Å^3$, which are substantially larger than those

reported for the $Mg_{0.75}Al_{0.5}Si_{0.75}O_3$ *LN*–type phase (a = b = 4.8194(3) Å, c = 12.6885(8) Å, V = 255.23(3) Å^3; Ishii et al., 2017). More than 900 unique reflections were collected and indexed in the space group *R3c* (#161) with R_{int} = 2.9%. A structure solution based on the single crystal data was further refined in an anisotropic approximation for all atoms to R_1 = 5.9%. The scattering factors of Mg, Al, and Si are similar, but very different to those of Fe. By assuming that both cation sites are fully occupied, we found that Fe^{3+} is located only in A site together with Mg. These results are in agreement with the Mössbauer spectroscopy data. Free refinement of the *A*-site occupancy yileds 0.48 (5) and 0.52 (5) for Mg and Fe^{3+}, respectively, which agrees with results of the chemical analysis. These two occupancies are indistinguishable from 0.5 within the uncertainties of this method. In the final structural refinement, we fixed the occupancies of Fe^{3+} and Mg in the *A*-site to 0.5. Since Si and Al in the *B* site cannot be distinguished by SXRD, their occupancies were also fixed to 0.5 based on the composition.

As shown in Figure 2, the $Mg_{0.5}Fe^{3+}_{0.5}$ and $Si_{0.5}Al^{3+}_{0.5}$ atoms occupy six-coordinated *A*- and *B*-sites to form AO_6 and BO_6 octahedra, respectively, which are interpenetrated via edge-sharing octahedral dimers in the *ab*-plane and face-sharing octahedral pairs along the *c*-axis. The size of the AO_6 octahedron (~10.3 Å^3) is significantly larger than that of the BO_6 octahedron (~8.6 Å^3) because AO_6 and BO_6 octahedra are occupied by larger (Mg^{2+} and Fe^{3+}) and smaller (Si^{4+} and Al^{3+}) cations, respectively. Noticeable structural features include the distortions of AO_6 and BO_6 octahedra as a result of shifts of *A* and *B* cations from the geometrical centers of face-sharing octahedra by 0.2 and 0.3 Å, respectively (see deposited CIF). The average bond lengths of two types of <Mg/Fe-O> are 1.975 ± 0.006 and 2.090 ± 0.008 Å, which are significantly larger than those of <Si/Al-O> (1.939 ± 0.008 and 1.802 ± 0.006 Å). We estimated the octahedral distortion using the above bond lengths by the following equation:

145 $$\Delta = \frac{1}{6}\sum_i \left\{\frac{(d_i - d_{ave})}{d_{ave}}\right\}^2, \quad (1)$$

146 where d_i is the individual bond length and d_{ave} is the average bond length. Values of Δ are 8×10^{-4}
147 and 13×10^{-4} for $(Mg_{0.5}Fe^{3+}_{0.5})O_6$ and $(Si_{0.5}Al^{3+}_{0.5})O_6$ octahedra, respectively, confirming a
148 weaker distortion of AO_6 than BO_6. Furthermore, the distortion of BO_6 octahedra in the present
149 phase is significantly larger than that of $MgSiO_3$ bridgmanite (1.6×10^{-5}) by a factor of 86.

150 We also use the Goldschmidt tolerance factor (*t*) for *LN*-type or perovskite ABO_3
151 compounds to express the geometric stability and crystal structure distortions in terms of
152 constituent ionic packing (Goldschmidt, 1926). The parameter *t* is defined by the ratios of
153 constituent ionic radii of *A*, *B* and O as $t = (r_A + r_O)/\sqrt{2}(r_B + r_O)$, where r_A, r_B, and r_O are
154 the ionic radii of *A* and *B* in six-fold coordination and O, respectively. As shown in Figure 3, we
155 obtained *t = 0.79* for $(Mg_{0.5}Fe^{3+}_{0.5})(Si_{0.5}Al^{3+}_{0.5})O_3$ (r_{Mg2+} = 0.72 Å; r_{Al3+} = 0.535 Å; r_{Fe3+} = 0.645
156 Å ; r_O = 1.4 Å) in the present study, which is comparable with that of *LN*-type $MnTiO_3$ (*t = 0.79*,
157 Ross et al., 1989), $Mg_{0.75}Al_{0.5}Si_{0.75}O_3$ (*t* = 0.80, Liu et al., 2016, 2017a; Ishii et al., 2017) but
158 significantly higher than that of $FeTiO_3$ (*t* = 0.77, Leinenweber et al., 1991). All of these values
159 are significantly lower than those for stable perovskite of $CaSiO_3$ (*t* = 0.95, Liu and Ringwood,
160 1975) and $MgSiO_3$ (*t = 0.*83, Ito and Matsui, 1978). In summary, *t* decreases with increasing *B*
161 cation radius relative to that of the *A* cation as a result of the increasing degree of cell distortion.

162

163 **IMPLICATIONS**

164 Most *LN*-type phases are generally accepted as a quenchable phase that back-transforms
165 from a high-pressure stable perovskite phase by a diffusionless transition because of the

displacement of A cations and distortion of BO_6 octahedra resulting from cation substitution upon decompression (e.g., Navrotsky et al., 1998; Ross et al., 1989; Leinenweber, 1991; Ishii et al., 2017). It is noted that the charge-coupled $FeAlO_3$ component dominates in bridgmanite, especially Fe^{3+}- and Al^{3+}-rich bridgmanite, although trace amounts of the oxygen vacancy substitution may exist in Fe^{3+}- and Al^{3+}-poor bridgmanite in the (Mg, Fe^{2+})O-$Fe^{3+}AlO_3$-SiO_2 ternary system (Fig. 4) (McCammon, 1997; Lauterbach et al. 2000; Frost and Langenhorst, 2002; Nishio-Hamane et al., 2005; Saikia et al., 2009; Boffa Ballaran et al. 2012; Yoshino et al., 2016). The Al_2O_3 content (25 mol%) in the present phase is also considerably higher than that in the Fe-free bridgmanite (12 mol%, Liu et al., 2016; 2017a). Therefore, the Al_2O_3 content in bridgmanite could be highly enhanced in the presence of Fe^{3+} because of the formation of the charge-coupled $Fe^{3+}AlO_3$ composition. In the present study, bridgmanite can incorporate the $FeAlO_3$ content up to 50 mol% at 27 GPa and 2000 K, which is beyond solubility limit in both pyrolite (~6 mol%)and MORB (mid-ocean ridge basalt) (~25 mol%) and previously reported value (37 mol%，Boffa Ballaran et al., 2012). Bridgmanite would thus be the major phase for Fe^{3+} and Al^{3+} for the pyrolite and MORB lower mantle.

Furthermore, the pressure at which the present phase forms (27 GPa) is significantly lower than that of the pyropic ($Mg_3Al_2Si_3O_{12}$ pyrope) *LN*-type phase (45 GPa, Liu et al., 2016; 2017a). This observation may be explained by a reduction of the ionic radius ratio between the A-site cation and oxygen because of the smaller Fe^{3+} in A (Mg) site and larger octahedral distortion than found in the pyropic *LN*-type phase. Our results together with that obtained by Boffa Ballaran et al. (2012) suggest that bridgmanite with the $FeAlO_3$ content above ~37 mol% would transform into the *LN*-type phase upon decompression from lower mantle conditions.

The formation of the *LN*–type phase is a useful indicator for constraining the pressure and temperature conditions for shocked meteorites (Sharp et al., 1997; Xie et al., 2006; Tomioka and Fujino 1997; Ishii et al., 2016). Dubrovinsky et al. (2009) found a natural *LN*–type $FeTiO_3$ phase from the Ries Crater, Germany, which is considered to be recovered from perovskite at 15-28 GPa after shocking (Akaogi et al., 2016). The presence of the Fe^{3+}-and Al^{3+}-rich *LN*–type phase can therefore be used to constrain the formation conditions of shocked meteorites.

Acknowledgements

The authors thank D. Krauße, H. Fischer, and S. Übelhack for their assistance with high-pressure assembly preparation. We also thanks for the editor Ian Swainson for processing our manuscript and four reviewers for constructive comments. Z. L. was financially supported by the Bayerisches Geoinstitut Visitors' Program. This study was also supported by research grants to T. K. (BMBF: 05K13WC2, 05K16WC2; DFG: KA3434/3-1, KA3434/7-1, KA3434/8-1, KA3434/9-1), L. D. (DU393/9-2, DU393/13-1), and C. M. (MC3/20-2). This project has received funding from the European Research Council (ERC) under the European Union's Horizon 2020 research and innovation programme (Proposal No. 787 527). J. G. C. is supported by the National Key R&D Program of China (Grant No. 2018YFA0305700), the National Science Foundation of China (Grant No. 11574377, 11874400), and the Key Research Program of Frontier Sciences (Grant No. QYZDB-SSWSLH013).

References

209 Abrahams, S. C., and Bernstein, J. L. (1967) Ferroelectric lithium tantalate—1. single crystal X-ray
210 diffraction study at 24 C Journal of Physics and Chemistry of Solids, 28, 1685.

211 Akaogi, M., Abe, K., Yusa, H., Ishii, T., Tajima, T., Kojitani, H., Mori, D., and Inaguma, Y. (2016) High-
212 pressure high-temperature phase relations in $FeTiO_3$ up to 35 GPa and 1600°C. Physics and
213 Chemistry of Minerals, 44, 63–73.

214 Dubrovinsky, L.S., El Goresy, A., Gillet, P., Wu, X., and Simionivici, A. (2009) A novel natural shock-
215 induced high-pressure polymorph of $FeTiO_3$ with the Liniobate structure from the Ries Crater,
216 Germany. Meteoritics and Planetary Science Supplement, 72, 5094.

217 Frost, D. J., and Langenhorst, F., (2002) The effect of $AlO_{1.5}$ on Fe–Mg partitioning between
218 magnesiowüstite and magnesium silicate perovskite. Earth and Planetary Science Letters, 199,
219 227–241.

220 Funamori, N., Yagi, T., Miyajima, N., and Fujino, K. (1997) Transformation in garnet: from
221 orthorhombic perovskite to $LiNbO_3$ phase on release of pressure. Science, 275, 513–515.

222 Goldschmidt, V. M. (1926) Naturwissenschaften, 14, 477.

223 Ishii, T., et al. (2016) Generation of pressure over 40 GPa using Kawai–type multi–anvil press with
224 tungsten carbide anvils. Review of Scientific Instruments, 87, 024501–1–024501–6.

225 Ishii, T., Sinmyo, R., Komabayashi, T., Boffa-Ballaran, T., Kawazoe, T., Miyajima, N., and Katsura, T.
226 (2017). Synthesis and crystal structure of $LiNbO_3$-type $Mg_3Al_2Si_3O_{12}$: A possible indicator of shock
227 conditions of meteorites. American Mineralogist, 102(9), 1947–1952.

228 Ito, E., and Matsui, Y. (1978) Synthesis and crystal–chemical characterization of $MgSiO_3$ perovskite.
229 Earth and Planetary Science Letters, 38, 443-450.

230 Ko, J., and Prewitt, C. T. (1988) High-pressure phase transition in $MnTiO_3$ from the ilmenite to the
231 $LiNbO_3$ structure. Physics and Chemistry of Minerals, 15, 355–362.

232 Lauterbach, S., McCammon, C. A., van Aken, P., Langenhorst, F., and Seifert, F., (2000) Mössbauer and
233 ELNES spectroscopy of $(Mg,Fe)(Si,Al)O_3$ perovskite: a highly oxidised component of the lower
234 mantle. Contributions to Mineralogy and Petrology, 138, 17–26.

235 Leinenweber, K., Utsumi, W., Tsuchida, Y., Yagi, T., and Kurita, K. (1991) Unquenchable high-pressure
236 perovskite polymorphs of $MnSnO_3$ and $FeTiO_3$. Physics and Chemistry of Minerals, 18, 244–250.

Liu, L., and A. E. Ringwood (1975) Synthesis of a perovskite-type polymorph of $CaSiO_3$. Earth and Planetary Science Letter, **14**, 209–211.

Liu, Z. D., Irifune, T. Nishi. M., Tange, Y., Arimoto, and T., Shinmei, T. (2016) Phase relations in the system $MgSiO_3$– Al_2O_3 up to 52 GPa and 2000 K. Physics of the Earth and Planetary Interiors, 257, 18–27.

Liu, Z. D., Nishi. M., Ishii, T., Fei, H. Z., Miyajima, N., Boffa Ballaran, T., Ohfuji, H., Sakai, T., Wang, L., Shcheka, S., Arimoto, T., Tange, Y., Higo, Y., Irifune, T., and Katsura, T. (2017a) Phase relations in the system $MgSiO_3$–Al_2O_3 up to 2300 K at lower-mantle pressures, Journal Geophysics Research, 10, 7775-7788.

Liu, Z. D., Ishii, T., and Katsura, T. (2017b) Rapid decrease of $MgAlO_{2.5}$ component in bridgmanite with pressure, Geochemical Perspective Letters, 5, 12-18.

McCammon, C.A. (1994) Mössbauer spectroscopy of quenched high-pressure phases: investigating the Earth's interior. Hyperfine Interact. 90, 89–105.

McCammon, C. A. (1997) Perovskite as a possible sink for ferric iron in the lower mantle. Nature, 387, 694–696.

Megaw, H.D., 1968. A note on the structure of lithium niobate, $LiNbO_3$. Acta Crystallographica A 24, 583e588.

Miyajima, N., Fujino, K., Funamori, N., Kondo, T., and Yagi, T. (1999). Garnet-perovskite transformation under conditions of the Earth's lower mantle: An analytical transmission electron microscopy study. Physics of the Earth and Planetary Interiors, 116(1–4), 117–131.

Navrotsky, A. (1998) Energetics and crystal chemical systematic among ilmenite, lithium niobate, and perovskite structures. Chemistry of Materials 10, 2787e2793.

Nishio-Hamane, D., Nagai, T., Fujino, K., Seto, Y., and Takafuji, N. (2005) Fe^{3+} and Al^{3+} solubilities in $MgSiO_3$ perovskite: implication of the Fe^{3+} AlO_3substitution in $MgSiO_3$ perovskite at the lower mantle condition. Geophysical Research Letter, 32, L16306.

Oxford Diffraction. CrysAlisPro. Oxford Diffraction Ltd, Abingdon, Oxfordshire, 2009, UK.

Sheldrick, G. M. A short history of SHELX, Acta Crystallographica, 2008, A64, 112–122

Farrugia, L. J. (1999) WinGX suite for small-molecule single-crystal crystallography. Journal of Applied Crystallography.

Ross, N. L., Ko, J., and Prewvitt, C.T. (1989) A new phase transition in $MnTiO_3$.: $LiNbO_3$-perovskite structure. Physics and Chemistry of Minerals, 16, 621-629.

Saikia, A., Boffa Ballaran, T., and Frost, D.J., 2009. The effect of Fe and Al substitution on the compressibility of $MgSiO_3$ perovskite determined through single-crystal X-ray diffraction. Physics of the Earth and Planetary Interiors, 173, 153–161.

Shannon, R.D. (1976) Revised effective ionic radii and systematic studies of interatomic distances in halides and chalcogenides. Acta Crystallographica A, 32, 751–767.

Sharp, T.G., Lingemann, C.M., Dupas, C., and Stöffler, D. (1997) Natural occurrence of $MgSiO_3$-ilmenite and evidence for $MgSiO_3$-perovskite in a shocked L chondrite. Science, 277, 352–355.

Tomioka, N. and Fujino, K. (1997) Natural $(Mg,Fe)SiO_3$-ilmenite and-perovskite in the Tenham meteorite. Science, 277, 1084–1086.

Xie, Z., Sharp, T. G. and DeCarlie, P. S. (2006) High-pressure phases in a shock-induced melt vein of the Tenham L6 chondrite: Constraints on shock pressure and duration, Geochimica et Cosmochimica Acta, 70, 504–515.

Yoshino, T., kamada, S., Chengcheng, Z., Ohtani, E., and Hirao, N. (2016) Electrical conductivity model of Al-bearing bridgmanite with implications for the electrical structure of the Earth's lower mantle. *Earth and Planetary Science Letters,* 434, 208-219.

Figures and Tables

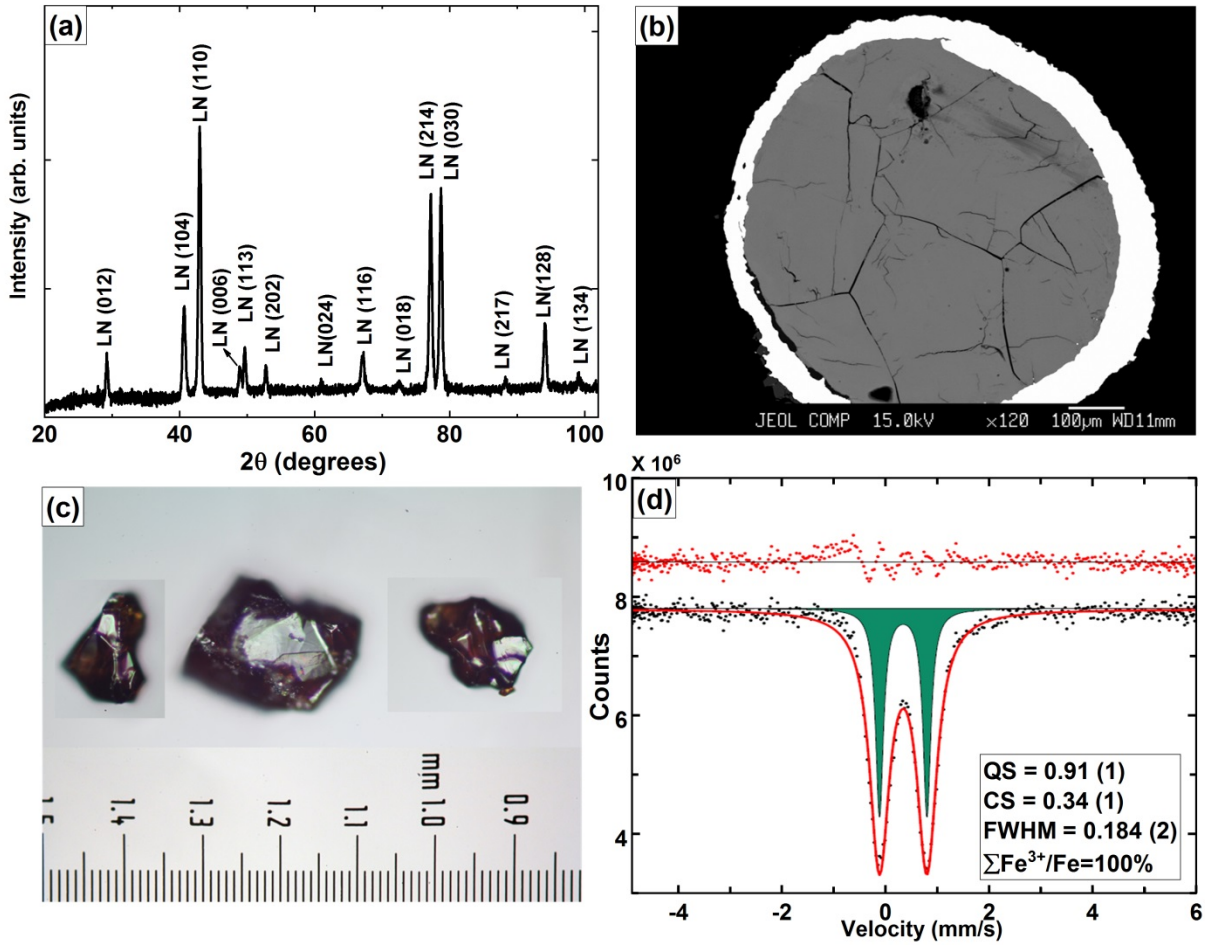

FIGURE 1. Characteristics of the $(Mg_{0.5}Fe^{3+}_{0.5})(Si_{0.5}Al^{3+}_{0.5})O_3$ *LN*–type phase: **(a)** MXRD profile, (**b**) BSE image, (c) photograph of selected single crystals, and (d) Mössbauer spectrum. Black dots indicate experimental data, while the red line shows the fitted curve. Red dots indicate the residual, i.e., the difference between calculated and experimental results. The small deviations in the residual are likely due to slight deviation from Lorentzian lineshape due to next-nearest-neighbor effects in the solid solution. Abbreviations: CS: center shift, QS: quadruple splitting, FWHM: Full width at half maximum.

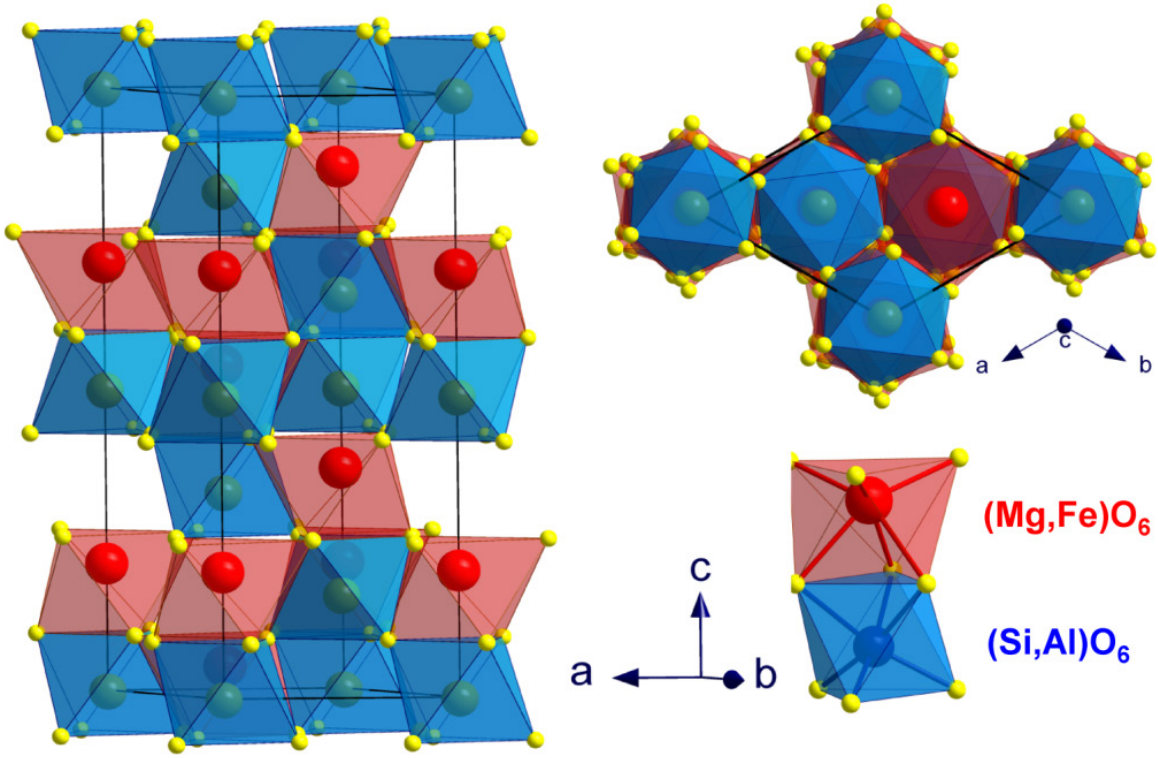

FIGURE 2. Crystal structure of the $(Mg_{0.5}Fe^{3+}_{0.5})(Si_{0.5}Al^{3+}_{0.5})O_3$ *LN*–type phase and AO_6 (A= $Fe^{3+}_{0.5}Mg_{0.5}$) and BO_6 (B = $Al^{3+}_{0.5}Si_{0.5}$) octahedra. Yellow spheres are oxygen, blue spheres are Si/Al^{3+}, and red spheres are Mg/Fe^{3+}.

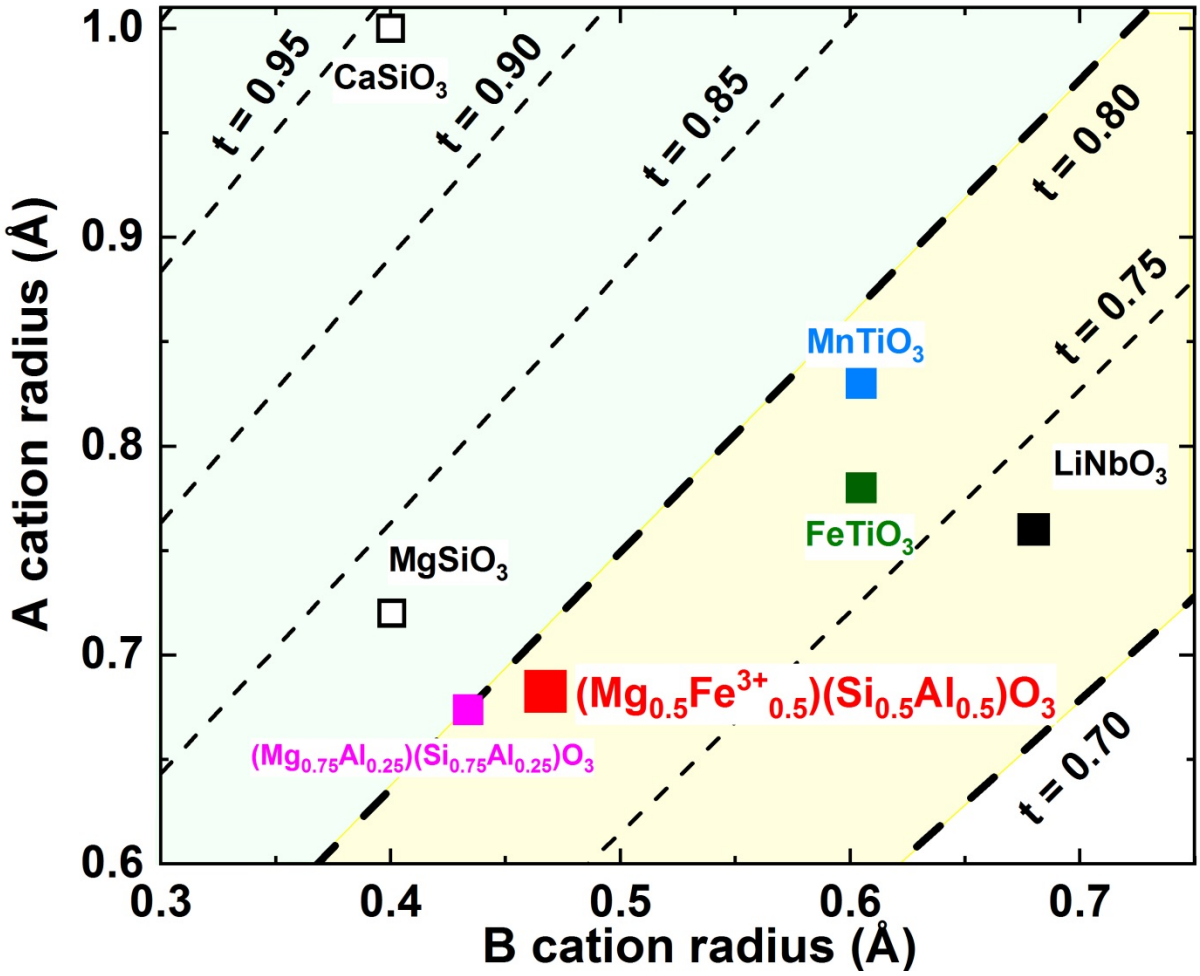

FIGURE 3. Goldschmidt diagram for selected ABO_3 perovskite and the *LN*-type compounds (yellow shading). Dotted lines are contours of the Goldschmit tolerance factor. Open symbols: perovskite-forming compounds ($CaSiO_3$: Liu and Ringwood, 1975; $MgSiO_3$: Ito and Matsui, 1978). Solid symbols: *LN*-type quenched products, $(Mg_{0.5}Fe^{3+}{}_{0.5})(Si_{0.5}Al^{3+}{}_{0.5})O_3$ (this study), $Mg_{0.75}Al_{0.5}Si_{0.75}O_3$ (Liu et al., 2016, 2017a; Ishii et al., 2017), $FeTiO_3$ (Akaogi e al., 2016), $MnTiO_3$ (Ko and Prewitt, 1988), and $LiNbO_3$ (Megaw, 1968).

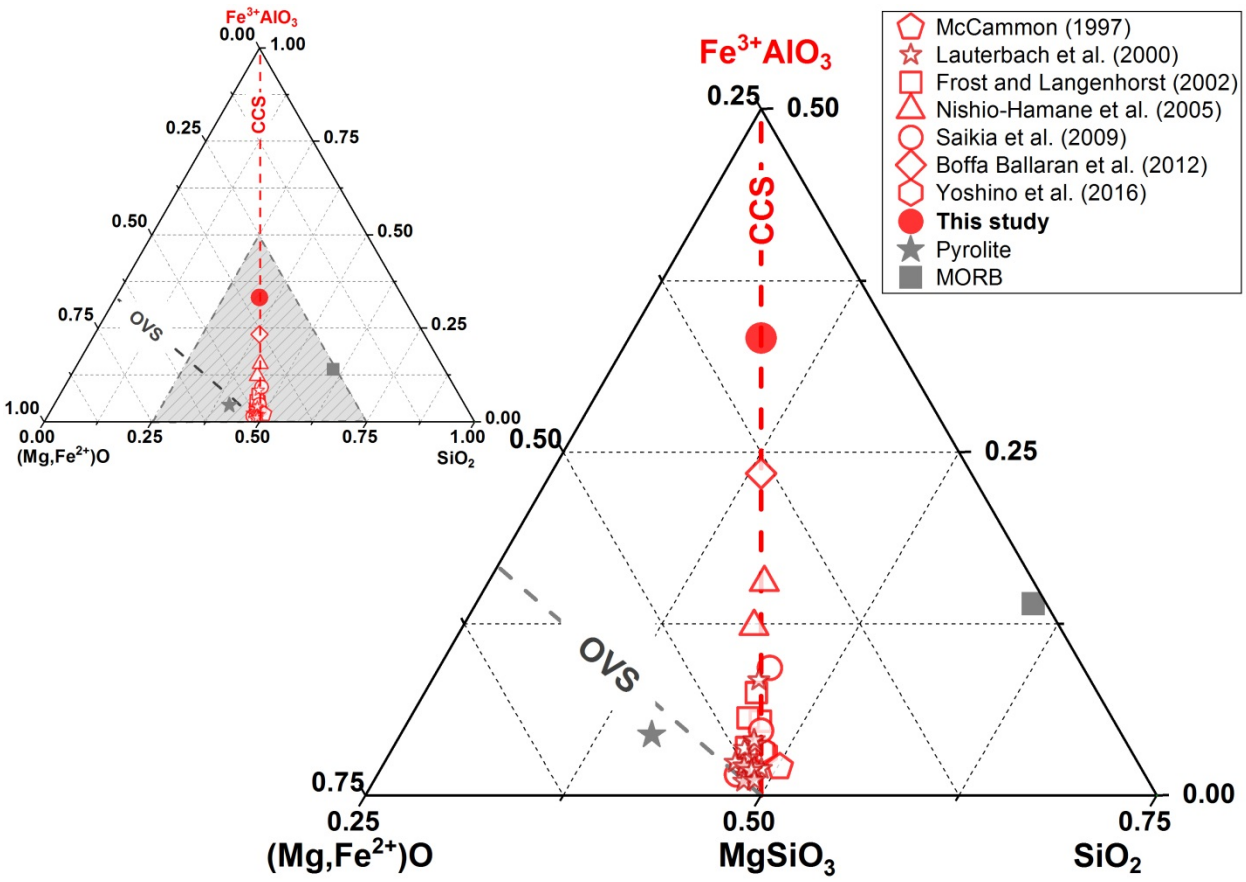

FIGURE 4. Ternary phase diagram of the (Mg, Fe^{2+})O-$Fe^{3+}AlO_3$-SiO_2 system for showing the compositions of Fe and Al-bearing bridgmanite in previous and present studies. The grey shadow is the magnified region from the whole ternary phase relations. The black star represents the composition of pyrolite by assuming the amount of Fe^{3+}/ΣFe of 50-60% under the reduced conditions (McCammon, 1997; Frost and Langenhorst, 2002), while the square represents that of MORB. Abbreviation: CCS, charge-coupled substitution (Mg^{2+} (A) + Si^{4+} (B) = M^{3+} (A) + M^{3+} (B), where M represent Fe^{3+} or Al^{3+}); OVS, oxygen vacancy substitution (2 Si^{4+} (B) + O^{2-} = 2M^{3+} (B) + V_o, where V_o is the oxygen vacancy).